RSC Advances

ROYAL SOCIETY OF CHEMISTRY

www.rsc.org/advances

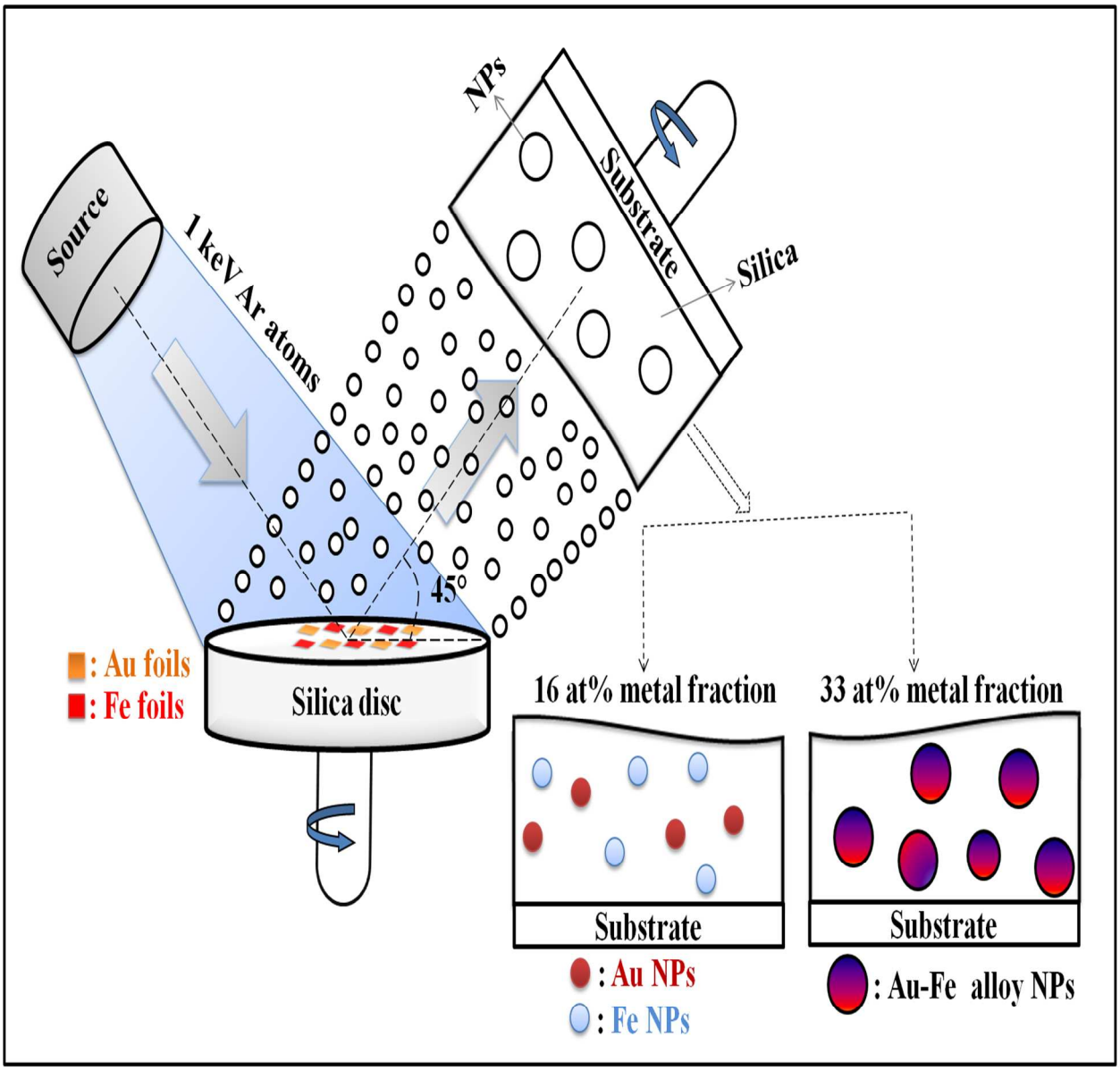

AuFe alloy nanoparticles (NPs) embedded in silica matrix is synthesized using atom beam sputtering setup. The increase in metal fraction in thin film from 16 at% to 33 at% results in the formation of alloy NPs.

Synthesis and characterization of Au-Fe alloy nanoparticles embedded in silica matrix by atom beam sputtering

Compesh Pannu[*1], Manju Bala[1], S. A. Khan[1], S. K. Srivastava[2], D. Kabiraj[1], D. K. Avasthi[1]

[1]Inter University Accelerator Centre, Aruna Asaf Ali Marg, New Delhi, India

[2]Department of Physics, Indian Institute of Technology Kharagpur, India

[*]Email: compesh@gmail.com

Abstract

In the present study we investigated the formation of AuFe alloy nanoparticles embedded in silica matrix by cosputtering of silica, Au and Fe with two different metal fractions using an atom beam source. The increase in metal fraction in the thin film results in the formation of AuFe alloy nanoparticles. The absence of surface plasmon resonance (SPR) for Au nanoparticles in optical spectrum, structural studies and transmission electron microscopy results confirmed existence of AuFe alloy nanoparticles. The nanocomposite is ferromagnetic at 2 *K* with a symmetric hysteresis loop. The formation of AuFe alloy nanoparticles in the thin film is explained on the basis of interatomic distance and diffusion phenomenon during deposition.

Keywords: Bimetallic nanoparticles, alloy, atom beam sputtering, X ray photo electron spectroscopy, X ray diffraction

Introduction

Bimetallic nanoparticles have different chemical and physical properties and superior features than their monometallic counterparts. In recent research scenario, bimetallic nanoparticles (NPs) have attracted substantial attention due to their manifold potential for application in several fields such as catalysis, biosensing, energy storage, data storage, magnetic resonance imaging, aerospace technology etc.[1-6] The enhanced catalytic properties of bimetallic nanoparticles have arouse significant interest in the field of chemical catalysis.[7] Bimetallic nanoparticles may form different structures such as core shell structures, heterostructures and alloy nanoparticles, depending on the metals, relative concentrations, and synthesis method.[8-9] It has been reported by several groups that solid /solid interface at the surface of an embedded nanoparticle provides extra degrees of control on the properties of nanoparticles.[10-12] For

example, contrary to the lowering of melting point observed for free standing clusters, Ge nanocrystals embedded in silica matrix reveal increase in melting point of nearly 200 K above the bulk value.[13] Metallic nanoparticles embedded in glass can increase the third order optical susceptibility of the composites by several orders of magnitude, making such materials an interesting candidate for optical switches.[14-15]

Most of the studies on bimetallic nanoparticles dispersed in a matrix involve metallic elements that are miscible. There are very few reports on the metallic elements that are immiscible in the bulk phase diagram. For the case of Au-Pt bulk phase diagram, there exist a miscible gap for Au-Pt bulk alloy.[16] In spite of that, the Au-Pt alloy nanoparticles can be synthesized in the whole composition range, which demonstrate that alloying mechanism[17] of nanosize materials is quite different from those of bulk counterparts. Recently it has also been shown that cosputtering of Co and Cu metals in silica matrix which are immiscible in bulk phase diagram forms alloy nanoparticles.[18] Therefore in the present study, our interest is to investigate bimetallic system Au and Fe which are immiscible metals in bulk phase. The pure Fe nanoparticles are magnetic in character and prone to oxidation which may lead to deterioration of magnetic properties. Au nanoparticles offers plasmonic properties that are tunable depending on the size, shape and surrounding medium.[19] Au-Fe alloy nanoparticles could merge optical and magnetic properties. Combining the optical and magnetic properties of Au and Fe in a single nanostructure would be useful in various applications for example in nanomedicine[20-21], information technology[22-24] and catalysis.[25]

At the nanoscale, the attempts to synthesize AuFe alloy have been limited so far. Formation of AuFe alloy nanoparticles is reported by Mattei et al using ion implantation technique in which Au and Fe were sequentially implanted in silica matrix.[26] AuFe nanoparticles

obtained by sequential ion implantation found to have problems with surface accessibility[27-28] which is important for catalytic applications.[24] In catalytic applications, surface accessibility (surface area accessible to the reactants) is directly related to the rate of product formation in a reaction and it follows that, the greater the amount of surface area accessible to the reactants, the larger is the throughput.[29] Therefore a new approach is needed that allows the synthesis of well dispersed and accessible nanoparticles. In the present work, we describe synthesis of AuFe alloy nanoparticles dispersed in silica matrix using atom beam sputtering technique. X ray photoelectron spectroscopy (XPS), X ray diffraction, UV Visible spectroscopy and Transmission electron microscopy have been carried out to confirm the existence of Au-Fe alloy nanoparticles in silica matrix.

1. Experimental Details

In the present study, Au and Fe were cosputtered along with silica for synthesis of nanocomposite thin films of silica containing metallic nanoparticles using atom beam sputtering technique.[30-32] A picture of the atom beam sputtering setup with geometrical details is shown in fig. 1. It consists of 1 keV Argon atom source which placed at an angle of 45˚ facing in the direction of sputtering target. The distance between Ar atom source and the sputtering target is 150 mm. A 3 inch diameter disc of pure SiO_2 with foils of Au and Fe glued on it was taken as sputtering target. The details of source, purity and thickness of Au and Fe foils used are given in table 1. The substrate holder was placed at an angle of 45° facing toward target surface and the distance between target and substrate holder is 150 mm. The substrate holder as well as target holder was rotated with the help of a DC motor at a speed of 5 rotations per minute for uniform sputtering and deposition of thin films. The base pressure and the sputter pressure of the chamber was $7x10^{-7}$ mbar and $4.6x10^{-3}$ mbar respectively. The atom source supplies a current of 30 mA

on the target. The relative area of silica disc, Au and Fe foils exposed to atom beam determines the amount of metal fraction in the thin film. Initially, a set of nanocomposite thin films with 16 at% metal fraction was deposited on quartz substrate. Subsequently, a second set of nanocomposite thin films on Silicon substrate with 33 at% metal fraction was prepared by increasing the relative area covered by Au and Fe foils on the silica disc. The metal fraction mentioned above represents the total composition of percentages of Au and Fe in the thin films. For convenience, hereafter the nanocomposite thin films with 16 at% and 33 at% metal fraction are designated as "A" and "B" respectively.

The thickness and metal content in the thin films were determined by Rutherford backscattering spectrometry (RBS) using 1.7 MeV tandem accelerator facility with 2 MeV He^+ ions. A silicon surface barrier detector was used at a backscattering angle of 165° and a solid angle of 1 msr. High resolution X ray diffraction (XRD) measurement of the thin films were carried out at Elletra (Italy) using synchrotron source with X ray energy of 15 keV to identify crystalline phases. The measurements were performed in θ-2θ geometry with step size of 0.005°/sec. X rays from synchrotron source are used as the conventional XRD (Cu Kα source) did not provide intense, sharp and well resolved data due to low intensity of X rays and limited resolution of setup. Optical absorbance spectroscopy of thin films was carried out in the wavelength range of 200 nm to 800 nm. The optical spectrum was recorded in the absorbance mode for thin films 'A' deposited on quartz substrate and in reflectance mode for the thin films 'B' deposited on Si substrate which are not transparent. The reflectance spectra is converted in to absorbance spectra using apparent absorbance log(1/R).[33] It provides a good representation of absorbance spectra. The X ray photo electron spectroscopy (XPS) was carried out using the PHI 5000 Verse Probe II system. The microfocussed Al Kα radiation (1486.6 eV) at 100 W power

was used for this study. In these conditions, the full width at half maximum of the Ag 3d5/2 line from a standard Ag sample was about 0.6 eV. The binding energy scale was referenced to C1s peak at 284.5 eV to correct the charging effects. For fitting the XPS spectra, the Shirley method of background correction was used. Transmission electron microscopy (TEM) study of thin films was carried out with 200 keV electrons using the JEOL JEM – 2010 (UHR) facility. The magnetic properties were measured at 2 *K* using a vibrating sample magnetometer (VSM) and applying a maximum field of 2 Tesla.

2. Results

It is well known that properties of nanocomposite thin films are highly correlated with the composition of the films. In the present work, RBS as well as SRIM code[34] (Stopping and Range of Ions in Matter) is employed to determine the composition of nanocomposite thin films. The RBS spectrum and depth profiles of the nanocomposite thin films A and B are shown in fig. 2 and fig. 3 respectively. The estimation of metal fractions and depth distribution was performed by simulation of RBS spectrum using Rutherford Universal Manipulation Program (RUMP) simulation code.[35] The total thickness of nanocomposite thin films and, Au and Fe atomic metal fractions are shown in table 2. The thicknesses of nanocomposite thin films A and B are 520 nm and 450 nm respectively.

In order to theoretically calculate the composition of films, sputtering yield of Au, Fe and SiO_2 was estimated from SRIM code. SRIM code is based on Monte Carlo simulation method. As the input sputtering parameters, it needs the incident ion (Ar), incident ion energy (1keV), incident angle (45°) and total number of ions (10,000). Sputtering yield (Y) of Au, Fe, Si and O calculated using SRIM code is shown in table 2. The atomic fraction of an element (Au and Fe) in a nanocomposite film is calculated by using the equation[36]

$$E_i = \frac{A_i Y_i}{A_{m1} Y_{m1} + A_{m2} Y_{m2} + A_{SiO_2}(Y_{Si} + Y_O)} \quad (1)$$

Where *i* stands for element (Au, Fe, Si and O) and M stands for metals only. The atomic fraction of Au and Fe calculated using equation 1 in comparison with RBS results is shown in table 3. It is clear from SRIM and RBS results that the measurements done using SRIM code overestimates the sputtering yield of elements.

Uv- Visible absorption spectrum of nanocomposite thin films A and B are shown in fig. 4(a) & 4(b) respectively. Both the spectra are recorded with bare substrate as a reference. The spectrum in fig. 4(a) contains a faint surface plasmon resonance (SPR) band at a wavelength of about 525 nm and the spectrum in fig. 4(b) does not show any SPR band. Basically SPR bands derive from the collective excitation of conduction electrons in nanoscale noble metals by annihilation of the incident photons and their resonance energy depends on the nanoparticle size, shape and interparticle separation as well as on chemical physical environment.[23] It is well known that pure Au nanoparticles in silica exhibit SPR band at about 530 nm[37] and Fe nanoparticles do not have a SPR in the visible range. Mattei et al[26] reported the sequential ion implantation of Au and Fe in silica and observed that due to AuFe alloying, optical absorption spectrum does not exhibit SPR of Au nanoparticles. In thin film A, the presence of faint Au SPR band indicates presence of isolated Au nanoparticles without any interaction with Fe atoms and thus indicating no alloy formation. The absence of Au nanoparticles SPR peak in the thin film B indicates that a strong electronic interaction between Au and Fe atoms occur which is able to damp the Au SPR band. Keeping in mind the interaction between Au and Fe atoms in thin film B, the AuFe alloy formation is inferred while in case of thin film A, there is no alloy formation during deposition.

Furthermore in order to confirm the alloy formation, XPS measurements were carried out using Al Kα radiation. The survey spectra of thin film 'A' and thin film 'B' displayed in fig. 5 reveal the presence of Au and Fe in both the films. The peak at 284.5 eV is the C 1s peak coming due to an unavoidable presence of hydrocarbons on the sample surface; all the XPS spectra, as mentioned earlier, have been charge referenced to this peak. The high resolution XPS spectra for thin film A and B in Au4f and Fe2p regions are shown in fig. 6 and fig. 7 respectively. Deconvoluting the Au (4f) region in fig. 6(a) shows that the main peak is located at 84.05 eV, the value of elemental Au. The other small peak is positioned at 85 eV, attributed to small Au clusters with diameters smaller than 2 nm.[38] For large clusters of diameters higher than 3 nm, the binding energy closely approximated to bulk metal value.[39] There is no signature of AuFe alloy in the spectrum. It is expected that due to low metal fraction in silica matrix, Au and Fe interaction during deposition does not take place. For the case of thin film B, deconvoluting the Au (4f) peak by curve fitting shows the presence of pure Au as well as an additional peak having 0.6 eV lower binding energy (as shown in fig. 6(b)). This is attributed to negative charge buildup on the Au atoms upon AuFe alloy formation as a result of Au (2.54) being more electronegative than Fe (1.83). Luo et al[40] reported the AuPd alloy formation and observed a negative shift of 0.2 eV in binding energy of $Au4f_{7/2}$ peak on alloying. Therefore in the present case, an additional peak in the Au4f region in fig. 6(b) is ascribed to AuFe alloy. The intensity of AuFe alloy peak indicates that alloyed fraction of Au with Fe is more than unalloyed pure Au. XPS peak fit parameters for thin film A as well as B are given in table 4. XPS spectra in the Fe 2p region in Fig. 7 shows the presence of Fe_2O_3 in thin film 'B'.

For morphological studies of AuFe alloy in thin film B, TEM measurements were carried out on the thin film. The morphology of the nanoparticles is shown in fig. 8(a) and corresponding

nanoparticle size distribution is shown in fig. 8(b). The average nanoparticle size is around 3 nm. All nanoparticles in thin film are more or less spherical in shape. Though some of the nanoparticles appear to be overlaying and interconnected, this is not really the situation because in planar TEM imaging projections of all nanoparticles from different depths appear in the image. To know the composition of these nanoparticles, EDX (energy dispersive X-ray) elemental mapping was performed on nanoparticles by selecting Au peak edge (83 eV) and Fe peak edge (708 eV). Au and Fe elemental mapping image is shown in fig. 8(c). It shows that Fe atoms present in the silica matrix as well as in the nanoparticles along with Au atoms. The Fe atoms present in the silica matrix may have formed iron oxide.

For structural studies of thin film B, XRD was performed using the synchrotron radiations. The diffraction pattern of the nanocomposite thin film B is shown in fig. 9. The diffraction pattern shows a face centered cubic (fcc) structure analogous to pure Au (111) at a 2θ angle of 20.15° and a peak corresponding to Fe_2O_3. The other reflection in thin film spectra is slightly at lower angle from pure Au (111) peak position. The lattice parameter of this peak is 0.412 nm which is slightly higher than the lattice parameter of pure Au (0.407 nm). This lattice parameter is also higher than that can be expected by simple rule of mixing of Au and Fe (Vegards law). The higher lattice parameter of AuFe alloy nanoparticles can be explained in terms of self interstitials.[41] A self interstitial is a type of point defect where a lattice atom occupies an interstitial site instead of its regular position.[42] Any interstitial site is smaller than its own atom size and presence of an atom at such interstitial site results in strain in the lattice surrounding it.

It is clear from the XRD pattern in fig. 9 that the as deposited AuFe alloy is Au rich. Some of the Fe atoms are present in the Au FCC lattice on the substitutional sites which in

principle contracts the lattice parameter due to the smaller size of Fe atoms. But in the present case the observed high lattice parameter suggests the presence of selfinterstitials too. Most of the Fe in the thin film which does not take part in alloy is present in the oxide form (Fe_2O_3) as shown in fig. 9 which matches well with the observations of XPS spectra in fig. 7 and TEM image in fig. 8.

The magnetic field dependence of the magnetization (*M*) of AuFe alloy nanoparticles in thin film B is measured using VSM at temperature of 2 *K*. Fig. 10 shows the variation of magnetization M as a function of external magnetic field H. The spectra was corrected for the diamagnetic contribution of silicon substrate and normalized to the total number of Fe atoms in thin film B measured using RBS. The magnetization versus magnetic field plot measured at the temperature 2 *K* (Fig. 10) shows that M linearly increases with applied magnetic field with a symmetric hysteresis loop showing ferromagnetic behavior of AuFe alloy. The inset of fig. 10 shows the enlarged view of the hysteresis loop from the centre. The coercivity and retentivity of hysteresis loop is 53 Oe and $5.6x10^{-4}$ Am^2/g respectively. Guire et al[43] measured the dependence of magnetic moment per Fe atom as a function of Au_xFe_{100-x} composition in melt spinning alloys and observed a decrease in magnetic moment per Fe atom for larger Au content in the alloy. Amendola et al[44] reported the value of magnetic moment per Fe atom as 0.01 Am^2/g for $Au_{89}Fe_{11}$ nanoalloys which is in close agreement with the present results and suggests that the composition of the AuFe alloy obtained in the present work should be enriched in Au.

3. Discussion

In order to understand the formation and growth of nanoparticles in thin films A and B, we start with evaluating the flux of sputtered species (Au, Fe, SiO_2) arriving at the substrate. It has been reported that the angular distribution of the ejected species follow in general, a nearly

cosine distribution although over/under cosine distribution may be observed depending on the energy of incident Ar atoms, angle of incidence and target type.[45-47] In the present case, the Ar atom beam source bombards the target with a flux of 5×10^{15} atoms cm^{-2} s^{-1} corresponding to a beam current of 30 mA. The incident flux of the sputtered species reaching to the substrate surface is an important parameter as it decides the effective time the surface atoms get for diffusion before getting covered by afterwards arriving species. The incident flux of sputtered species can be estimated by sputtering yield but a fraction of the sputtered species get desorbed after reaching to substrate surface and therefore it is difficult to calculate the actual incident flux. Apart from this, the scattered Ar atom of energy 1 keV may also hit the substrate/film. However, quite a good estimation of incident flux can be done from film deposition rate. In the present case, film deposition rate is few tens of monolayer per minute, and thus the incident flux of metallic species on substrate surface is about 6×10^{13} atoms cm^{-2} s^{-1}. The kinetic energy of these sputtered species influences the structure and morphology of the thin film. Kinematic theory shows that higher the mass of the sputtered species lower will be its kinetic energy. The mean kinetic energy of Au and Fe sputtered atoms calculated by TRIM code is 20 eV. This energy is dissipated in the thin film and increase the local transient temperature of the film at the landing points. This temperature rise may lead to a transiently spatiotemporal enhancement of surface migration of adatoms and chemical interaction between the landing species. Khan et al[48] indicated that the species of incident energy of 1-100 eV can create a transient temperature rise of 1000 K in a radius of 0.5 – 2 nm for few picoseconds.

The growth of thin film using atom beam sputtering take in to account the following basic processes: (i) absorption and desorption of atoms on the substrate surface (ii) diffusion of deposited atoms on surface (iii) clustering of atoms leading to nucleation and growth of

nanoparticles[49]. However formation of nanoparticles depends on the average interatomic distance (d_{avg}) of atoms in the thin film, which is a function of areal coverage of Au and Fe foils on the SiO_2 target. The interatomic distance is calculated using the RBS results. In the present calculation, it is assumed that Au and Fe atoms in the thin film are identical and point like objects. If we take an atom as the centre and draw a sphere of radius r such that it is in contact with maximum number of like spheres, therefore the available space is filled very efficiently. In this way, the interatomic distance is d. The value of d can be evaluated as

$$N * volume\ of\ a\ sphere = volume\ of\ thin\ film \qquad (2)$$

Where N is total number of atoms in thin film. Using equation 1, the estimated values of d are 0.48 nm and 0.63 nm for thin films A and B respectively. The nucleation and growth of nanoparticles occurs when

$$d < L_d$$

where L_d is diffusion length of metal atoms. The relative diffusion length (L_d) of the adatoms can be calculated as[50]

$$L_d = \sqrt{D * t} \approx \sqrt{\frac{D}{\Theta_m}} \approx \sqrt{\frac{\exp\left(\frac{E}{RT}\right)}{\Theta_m}} \qquad (3)$$

Where D is diffusion coefficient, Θm is flux of incident metallic species on substrate surface, E is activation energy of metal atom on SiO_2 surface [48], R is gas constant and T is substrate temperature. In the present case, calculated diffusion length L_d of Au atoms on surface of SiO_2 is ≈ 0.5 nm. For simplicity it is assumed that the diffusion length of Fe atoms on surface of SiO_2 is also ≈ 0.5 nm. Au, Fe and SiO_2 altogether present in the thin films A and B, therefore following possibilities of interaction arise: (a) Au, Au (b) Au, Fe (c) Fe, Fe (d) Si, O (e) Fe, and O

The bond energy between Au-Au, Au-Fe, Fe-Fe, Si-O, and Fe-O atoms are 222, 187, 100, 809 and 408 kJ/mol respectively[51]. During sputtering, sputtered species may be in atomic or cluster form. Atoms landing on the surface are quite mobile and diffuse over the surface. These diffusing adatoms prefer sites with higher binding energies since this helps in lowering the potential energy of the system. Most of the Si and O atoms reaching the surface form SiO_2 molecule by surface reaction due to highest bond energy. Au atom diffusing on the surface of silica rich region will prefer to attach with Au adatom due to higher Au-Au bond energy compared to Au-Fe bond energy. If such sites are unavailable in the close vicinity, then Au adatom is trapped at nearest Fe site and hence AuFe alloy cluster nucleates. The further growth of Au cluster and alloy cluster takes place due to subsequent Au and Fe adatoms reaching close to these clusters before getting buried under subsequent silica deposits since silica is higher in concentration. It may be mentioned here that Au adatoms can also interact with Si atoms but availability of unreacted Si atoms on the surface is very low due to strong tendency of formation of SiO_2 molecules. Similarly diffusing Fe adatoms may react with O, Au and Fe with decreasing probability in that order. Fe adatoms have a stronger tendency to attach with nearby Oxygen atoms to form Iron oxide.

In case of set A, due to higher interatomic distance as compared to diffusion length, the probability of interaction of Au and Fe atoms with each other is very less. Even then if some atoms come in close vicinity then Au-Au prefers to bind as compared to Au-Fe due to higher bond energy. This suggests that small Au clusters nucleates during deposition (as confirmed by faint Au SPR peak in fig. 4(a) and XPS spectra in fig. 6(a)) and AuFe alloy nanoparticles are not formed or if they are formed, they are too small and few in number to be detected by different characterization techniques.

In case of set B, due to smaller interatomic distance as compared to set A, the probability of interaction of atoms is large. This suggests the formation of AuFe alloy nanoparticles along with Au nanoparticles during deposition which is quiet evident by XPS spectra in fig. 6(b) and XRD pattern in fig. 9.

4. Conclusion

Synthesis of thin films containing AuFe alloy nanoparticles embedded in silica matrix by atom beam sputtering technique has been studied. Two different metal fractions were cosputtered with silica. The composition and average interatomic distance between metal atoms in thin films are determined by RBS. It has been found that the thin films with interatomic distance less than the diffusion length of metal atoms results in to the formation of AuFe alloy nanoparticles. Optical, XPS and XRD results confirm the existence of these AuFe alloy nanoparticles in the thin film. The AuFe alloy in the thin film is observed to be magnetic in nature. Au and Fe interatomic distance and diffusion phenomenon during deposition plays a crucial role in formation of AuFe alloy nanoparticles.

5. Acknowledgement

One of the author (Compesh Pannu) would like to acknowledge University Grant Commission, India for providing financial support in form of fellowship. Author also thanks Dr. Santanu Ghosh, IIT Delhi for reflectance spectroscopy and AIRF, JNU for providing TEM facility and VSM measurements.

Figure captions

Fig. 1 Schematic of atom beam sputtering setup

Fig. 2 RBS spectra of a) thin film A, b) depth profile of different elements in the thin film A.

Fig. 3 RBS spectra of a) thin film B, b) depth profile of different elements in the thin film B.

Fig. 4 Uv-Visible absorption spectra of (a) thin film A, (b) thin film B

Fig. 5 A XPS survey spectra for thin film 'A' and thin film 'B'

Fig. 6 XPS spectrum in Au4f region of a) thin film A, b) thin film B

Fig. 7 XPS spectrum in Fe2p region of a) thin film A, b) thin film B

Fig. 8 TEM of thin film B (a) Image, (b) nanoparticle size distribution and (c) elemental mapping using EDS

Fig. 9 XRD pattern of nanocomposite thin film B

Fig. 10 M – H curve of the nanocomposite thin film B measured at 2 K

Table 1: Details of Source, purity and thickness of Au, Fe foils used.

Table 2: Thickness and atomic fraction of thin films calculated using RUMP simulation of RBS spectrum.

Table 3: Sputtering yield and atomic fraction of different elements using SRIM code simulation

Table 4: XPS peak fit parameters of thin film A and thin film B.

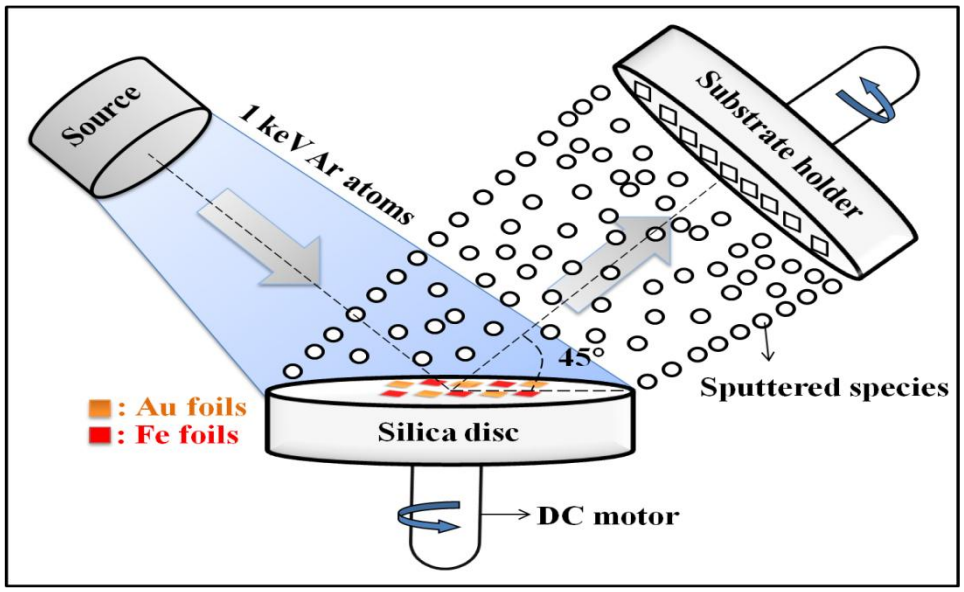

Fig. 1

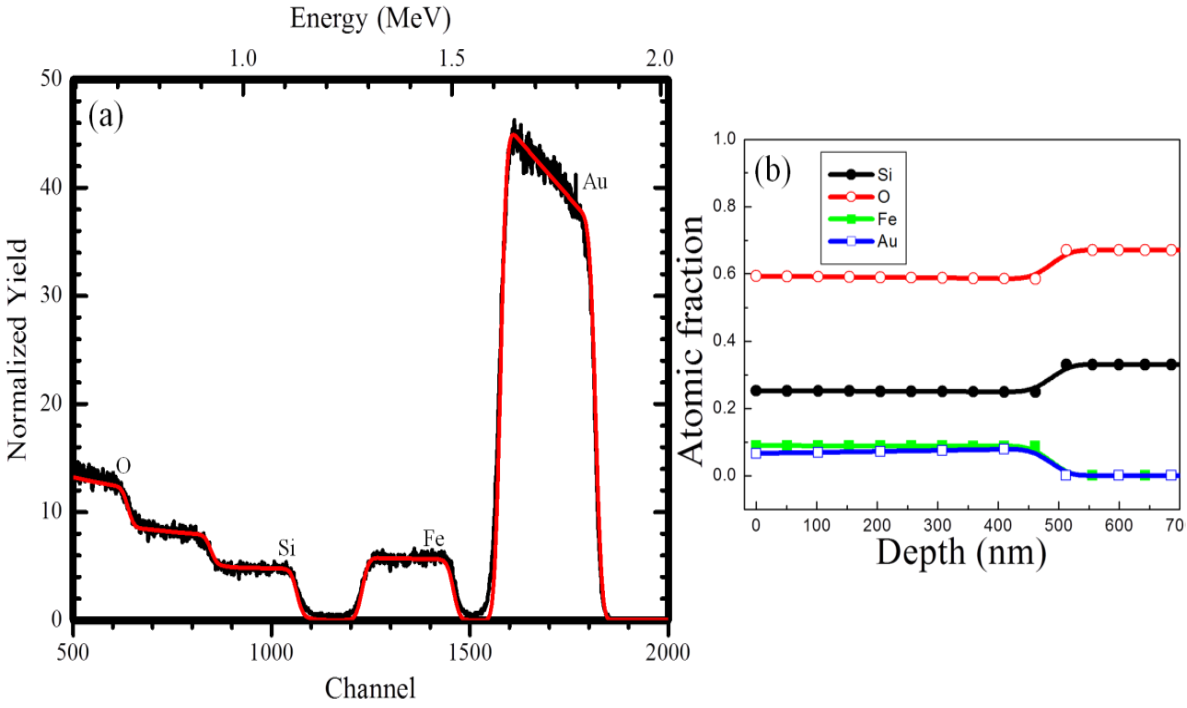

Fig. 2

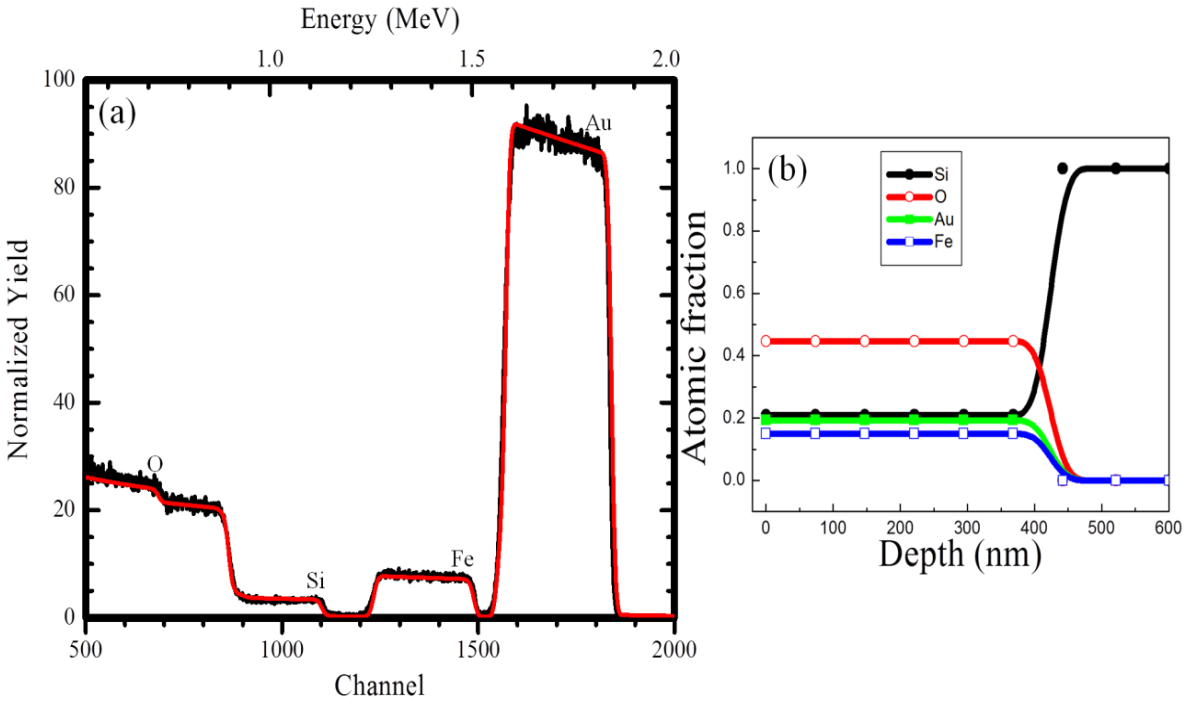

Fig. 3

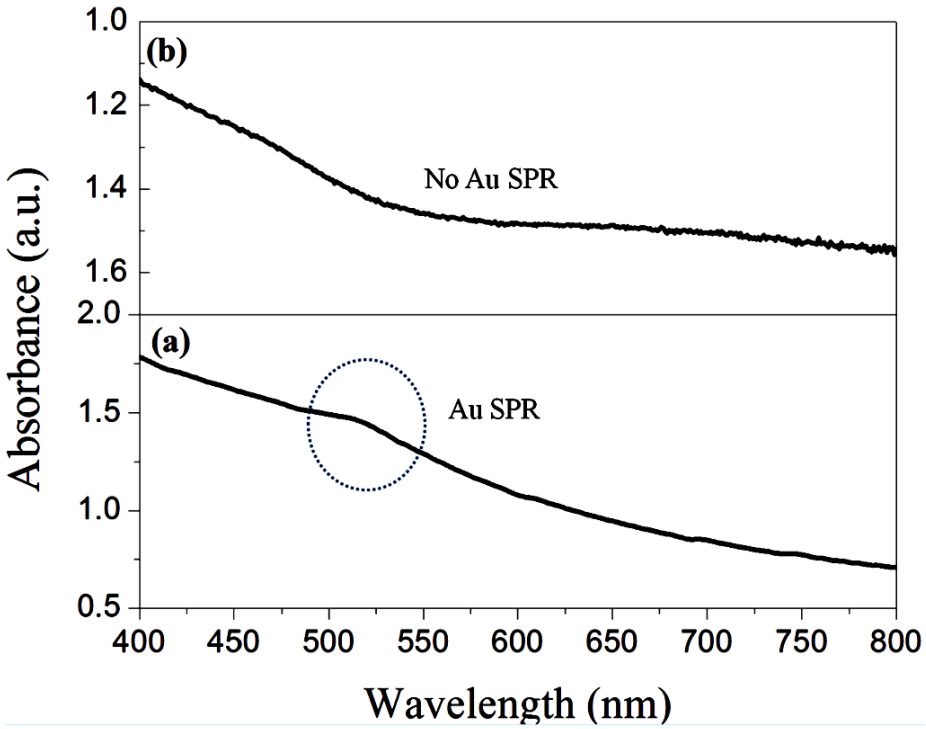

Fig. 4

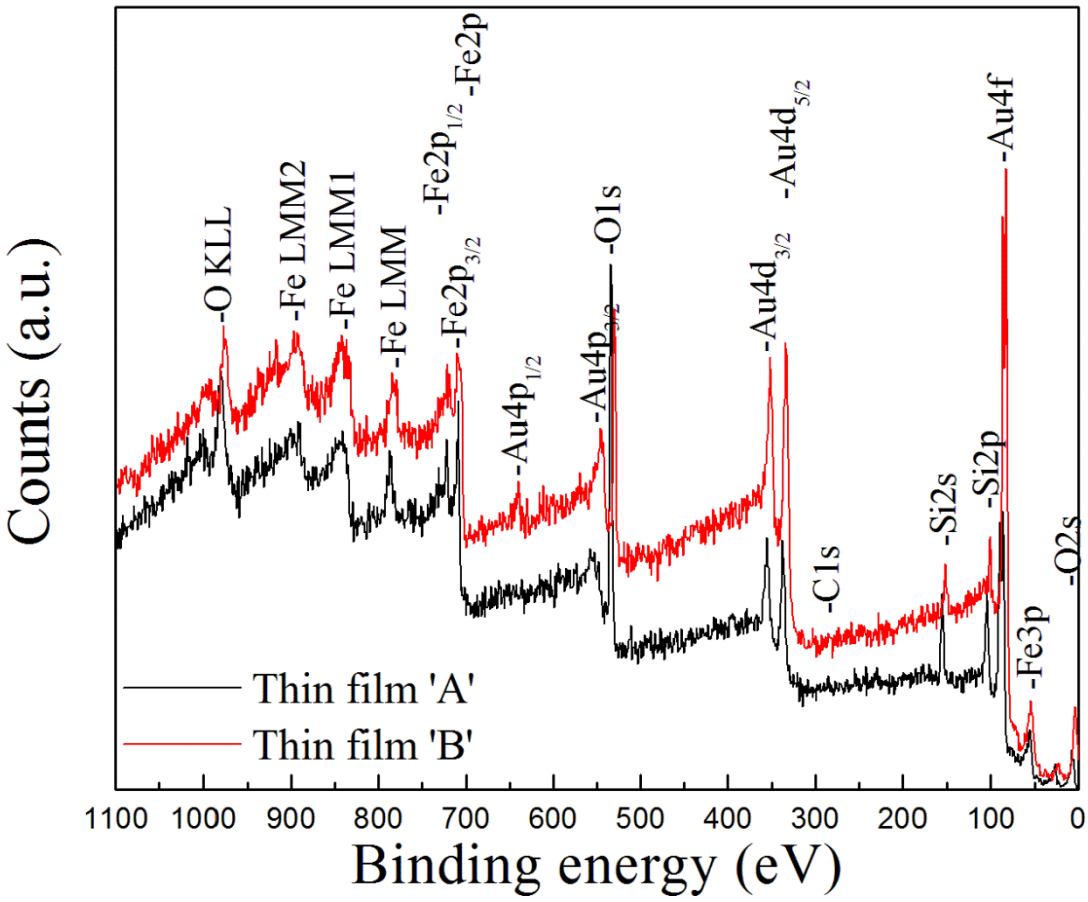

Fig. 5

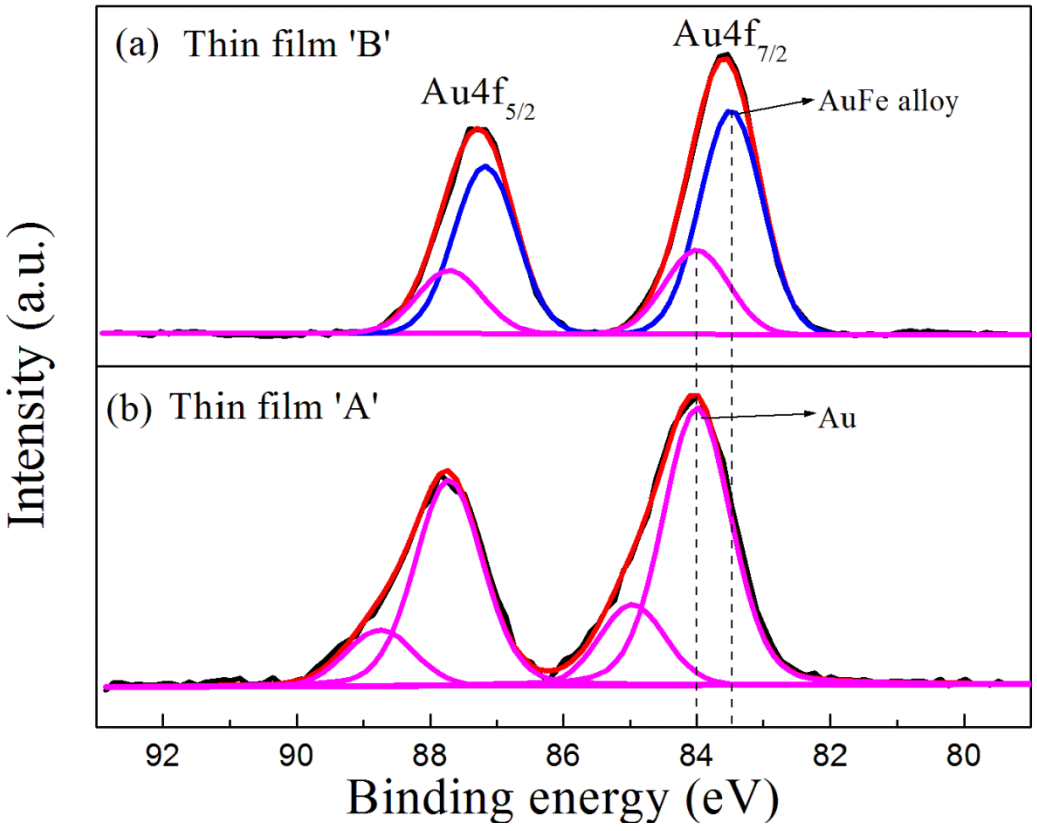

Fig. 6

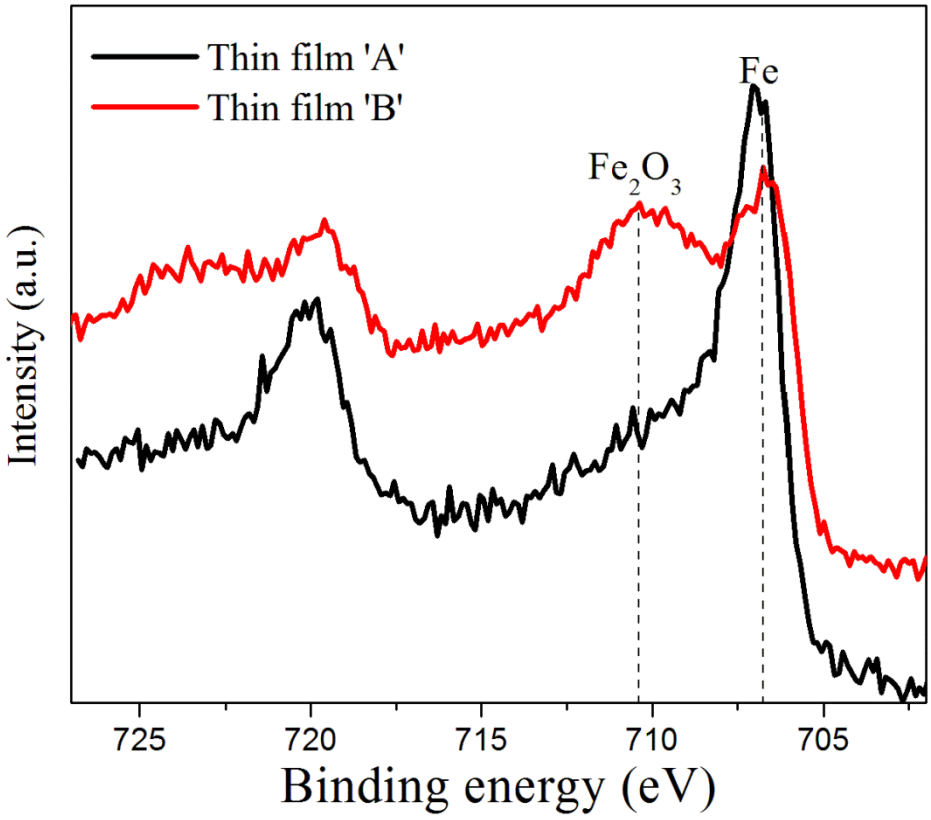

Fig. 7

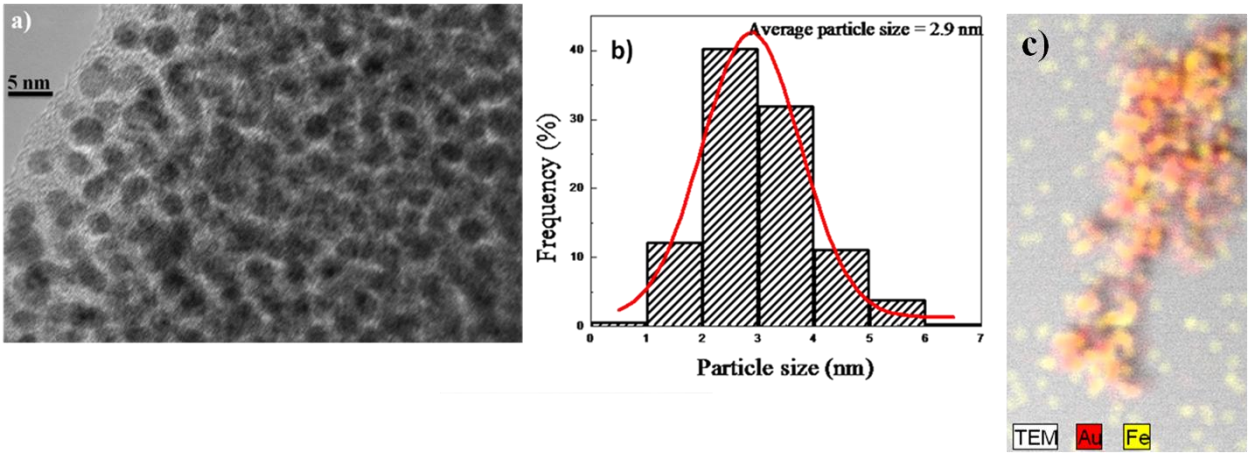

Fig. 8

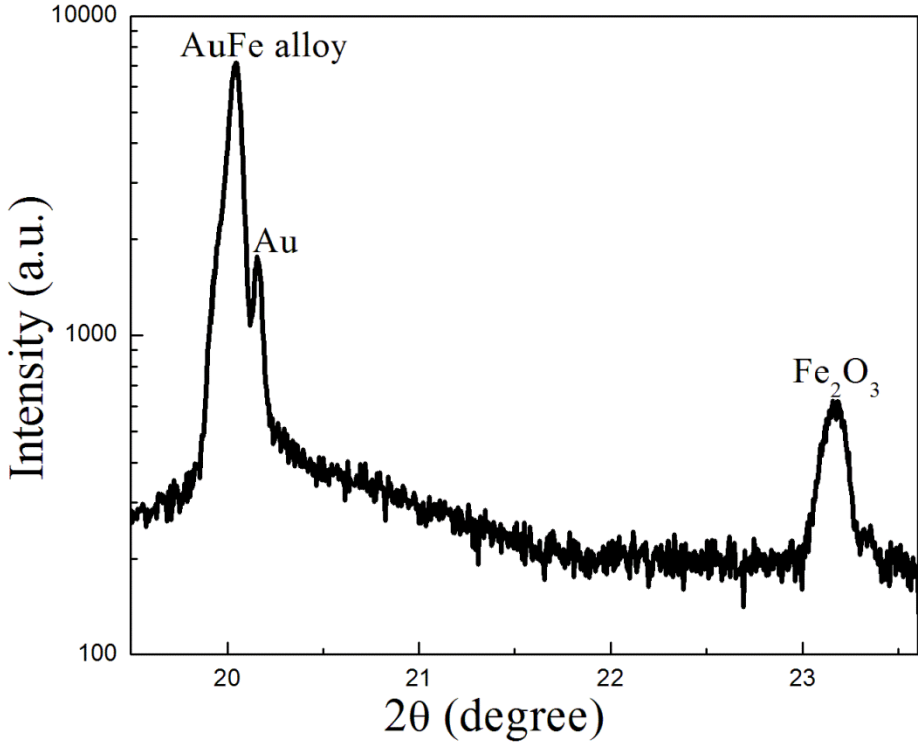

Fig. 9

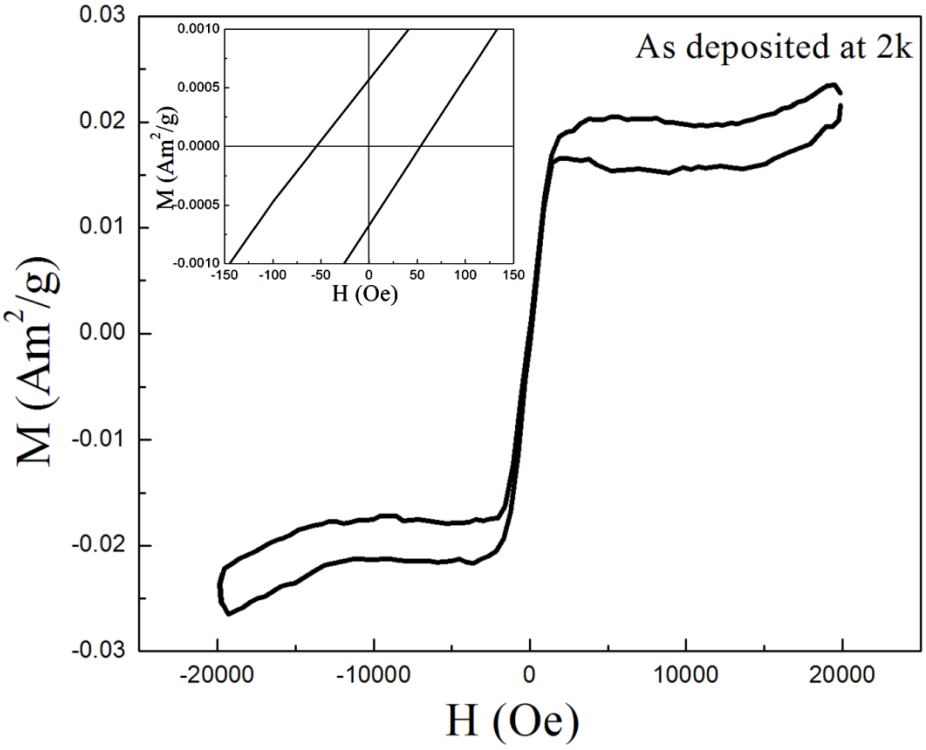

Fig. 10

Table 1:

Foils used	Area of each foil (mm^2)	Total no. of foils used	Thickness (mm)	Purity (%)	Source
Au	25	16	0.25	99.95	Aldrich
Fe	25	16	0.1	99.99	Aldrich

Table 2

Thin film	Thickness (nm)	Atomic fraction (%)	
A	520	Au	7.4
		Fe	8.8
		SiO_2	83.8
B	450	Au	19.2
		Fe	14.0
		SiO_2	66.8

Table 3

Thin film	Element	Area A_i (mm^2)	Sputtering yield Yi (atoms/ion)	Atomic fraction (%)
A	Au	150	4.3	8.6
	Fe	200	3.5	9.4
	SiO_2	1678	0.8 (Si), 2.9 (O)	82.0
B	Au	400	4.3	22.7
	Fe	400	3.5	18.5
	SiO_2	1228	0.8 (Si), 2.9 (O)	58.8

Table 4

Thin film		Peak 1 (eV)		Peak 2 (eV)	
		Centre	FWHM	Centre	FWHM
A	$4f_{7/2}$	84	1.2	85	1.18
	$4f_{5/2}$	87.7	1.2	88.75	1.2
B	$4f_{7/2}$	83.48	1.1	84	1.13
	$4f_{5/2}$	87.17	1.1	87.70	1.13

References

1. Ferrando, R.; Jellinek, J.; Johnston, R. L. Nanoalloys: from theory to applications of alloy clusters and nanoparticles. *Chemical Reviews* 2008, 108, 845-910.
2. Koh, S.; Leisch, J.; Toney, M. F.; Strasser, P. Structure-activity-stability relationships of Pt-Co alloy electrocatalysts in gas-diffusion electrode layers. *The Journal of Physical Chemistry C* 2007, 111, 3744-3752.
3. Lim, B.; Jiang, M.; Camargo, P. H.; Cho, E. C.; Tao, J.; Lu, X.; Zhu, Y.; Xia, Y. Pd-Pt bimetallic nanodendrites with high activity for oxygen reduction. *Science* 2009, 324, 1302-1305.
4. Gupta, G.; Slanac, D. A.; Kumar, P.; Wiggins-Camacho, J. D.; Wang, X.; Swinnea, S.; More, K. L.; Dai, S.; Stevenson, K. J.; Johnston, K. P. Highly stable and active Pt− Cu oxygen reduction electrocatalysts based on mesoporous graphitic carbon supports. *Chemistry of materials* 2009, 21, 4515-4526.
5. Greeley, J.; Stephens, I.; Bondarenko, A.; Johansson, T. P.; Hansen, H. A.; Jaramillo, T.; Rossmeisl, J.; Chorkendorff, I.; Nørskov, J. K. Alloys of platinum and early transition metals as oxygen reduction electrocatalysts. *Nature Chemistry* 2009, 1, 552-556.
6. Khanal, S.; Casillas, G.; Velazquez-Salazar, J. J.; Ponce, A.; Jose-Yacaman, M. Atomic Resolution Imaging of Polyhedral PtPd Core–Shell Nanoparticles by Cs-Corrected STEM. *The Journal of Physical Chemistry C* 2012, 116, 23596-23602.
7. Bhattarai, N.; Khanal, S.; Bahena, D.; Whetten, R. L.; Jose-Yacaman, M. In *Synthesis and Structural Characterization of Ferromagnetic Au/Co Nanoparticles*, MRS Proceedings, Cambridge Univ Press: 2014; pp mrss14-1708-vv06-03.
8. Einax, M.; Dieterich, W.; Maass, P. Colloquium: Cluster growth on surfaces: Densities, size distributions, and morphologies. *Reviews of modern physics* 2013, 85, 921.
9. Khanal, S.; Spitale, A.; Bhattarai, N.; Bahena, D.; Velazquez-Salazar, J. J.; Mejía-Rosales, S.; Mariscal, M. M.; José-Yacaman, M. Synthesis, characterization, and growth simulations of Cu–Pt bimetallic nanoclusters. *Beilstein Journal of Nanotechnology* 2014, 5, 1371-1379.
10. Sutter, E.; Sutter, P. Phase diagram of nanoscale alloy particles used for vapor-liquid-solid growth of semiconductor nanowires. *Nano letters* 2008, 8, 411-414.
11. Holmberg, V. C.; Panthani, M. G.; Korgel, B. A. Phase transitions, melting dynamics, and solid-state diffusion in a nano test tube. *Science* 2009, 326, 405-407.
12. Kim, B.; Tersoff, J.; Kodambaka, S.; Reuter, M.; Stach, E.; Ross, F. Kinetics of individual nucleation events observed in nanoscale vapor-liquid-solid growth. *Science* 2008, 322, 1070-1073.
13. Xu, Q.; Sharp, I.; Yuan, C.; Yi, D.; Liao, C.; Glaeser, A.; Minor, A.; Beeman, J.; Ridgway, M.; Kluth, P. Large melting-point hysteresis of Ge nanocrystals embedded in SiO 2. *Physical review letters* 2006, 97, 155701.
14. Mazzoldi, P.; Arnold, G.; Battaglin, G.; Gonella, F.; Haglund Jr, R. Metal nanocluster formation by ion implantation in silicate glasses: nonlinear optical applications. *Journal of Nonlinear Optical Physics & Materials* 1996, 5, 285-330.
15. Kreibig, U.; Vollmer, M. Optical properties of metal clusters. 1995.
16. Hultgren, R.; Desai, P. D.; Hawkins, D. T.; Gleiser, M.; Kelley, K. K. *Selected values of the thermodynamic properties of binary alloys*; DTIC Document: 1973.
17. Xiao, S.; Hu, W.; Luo, W.; Wu, Y.; Li, X.; Deng, H. Size effect on alloying ability and phase stability of immiscible bimetallic nanoparticles. *The European Physical Journal B-Condensed Matter and Complex Systems* 2006, 54, 479-484.
18. Mattei, G.; Battaglin, G.; Cattaruzza, E.; Maurizio, C.; Mazzoldi, P.; Sada, C.; Scremin, B. Synthesis by co-sputtering of Au–Cu alloy nanoclusters in silica. *Journal of Non-Crystalline Solids* 2007, 353, 697-702.

19. Kelly, K. L.; Coronado, E.; Zhao, L. L.; Schatz, G. C. The optical properties of metal nanoparticles: the influence of size, shape, and dielectric environment. *The Journal of Physical Chemistry B* 2003, 107, 668-677.
20. McCarthy, J. R.; Weissleder, R. Multifunctional magnetic nanoparticles for targeted imaging and therapy. *Advanced drug delivery reviews* 2008, 60, 1241-1251.
21. Gao, J.; Gu, H.; Xu, B. Multifunctional magnetic nanoparticles: design, synthesis, and biomedical applications. *Accounts of chemical research* 2009, 42, 1097-1107.
22. Belotelov, V.; Akimov, I.; Pohl, M.; Kotov, V.; Kasture, S.; Vengurlekar, A.; Gopal, A. V.; Yakovlev, D.; Zvezdin, A.; Bayer, M. Enhanced magneto-optical effects in magnetoplasmonic crystals. *Nature Nanotechnology* 2011, 6, 370-376.
23. Jain, P. K.; Xiao, Y.; Walsworth, R.; Cohen, A. E. Surface plasmon resonance enhanced magneto-optics (SuPREMO): Faraday rotation enhancement in gold-coated iron oxide nanocrystals. *Nano letters* 2009, 9, 1644-1650.
24. Wang, L.; Clavero, C.; Huba, Z.; Carroll, K. J.; Carpenter, E. E.; Gu, D.; Lukaszew, R. A. Plasmonics and Enhanced Magneto-Optics in Core− Shell Co− Ag Nanoparticles. *Nano letters* 2011, 11, 1237-1240.
25. Wang, D.; Li, Y. Bimetallic Nanocrystals: Liquid-Phase Synthesis and Catalytic Applications. *Advanced Materials* 2011, 23, 1044-1060.
26. Mattei, G.; de Julián Fernández, C.; Battaglin, G.; Maurizio, C.; Mazzoldi, P.; Scian, C. Structure and thermal stability of Au–Fe alloy nanoclusters formed by sequential ion implantation in silica. *Nuclear Instruments and Methods in Physics Research Section B: Beam Interactions with Materials and Atoms* 2006, 250, 225-228.
27. de Julián Fernández, C.; Mattei, G.; Paz, E.; Novak, R.; Cavigli, L.; Bogani, L.; Palomares, F.; Mazzoldi, P.; Caneschi, A. Coupling between magnetic and optical properties of stable Au–Fe solid solution nanoparticles. *Nanotechnology* 2010, 21, 165701.
28. Chiang, I. C.; Chen, D. H. Synthesis of monodisperse FeAu nanoparticles with tunable magnetic and optical properties. *Advanced Functional Materials* 2007, 17, 1311-1316.
29. Koch, C. C. *Nanostructured materials: processing, properties and applications*. William Andrew: 2006.
30. Avasthi, D.; Mishra, Y.; Kabiraj, D.; Lalla, N.; Pivin, J. Synthesis of metal–polymer nanocomposite for optical applications. *Nanotechnology* 2007, 18, 125604.
31. Kabiraj, D.; Abhilash, S.; Vanmarcke, L.; Cinausero, N.; Pivin, J.; Avasthi, D. Atom beam sputtering setup for growth of metal particles in silica. *Nuclear Instruments and Methods in Physics Research Section B: Beam Interactions with Materials and Atoms* 2006, 244, 100-104.
32. Pannu, C.; Singh, U. B.; Agarwal, D. C.; Khan, S. A.; Ojha, S.; Chandra, R.; Amekura, H.; Kabiraj, D.; Avasthi, D. K. A study on the consequence of swift heavy ion irradiation of Zn–silica nanocomposite thin films: electronic sputtering. *Beilstein Journal of Nanotechnology* 2014, 5, 1691-1698.
33. Kelly, S.; Hesterberg, D.; Ravel, B. Methods of soil analysis, Part 5, Mineralogical methods. *Soil Science Society of America, Medison* 2008, 387-463.
34. Ziegler, J. F.; Biersack, J. P. SRIM-2008, Stopping Power and Range of Ions in Matter. 2008.
35. Doolittle, L. R. A semiautomatic algorithm for Rutherford backscattering analysis. *Nuclear Instruments and Methods in Physics Research Section B: Beam Interactions with Materials and Atoms* 1986, 15, 227-231.
36. Kumar, H.; Mishra, Y.; Mohapatra, S.; Kabiraj, D.; Pivin, J.; Ghosh, S.; Avasthi, D. Compositional analysis of atom beam co-sputtered metal–silica nanocomposites by Rutherford backscattering spectrometry. *Nuclear Instruments and Methods in Physics Research Section B: Beam Interactions with Materials and Atoms* 2008, 266, 1511-1516.
37. Kan, C.; Cai, W.; Li, C.; Zhang, L.; Hofmeister, H. Ultrasonic synthesis and optical properties of Au/Pd bimetallic nanoparticles in ethylene glycol. *Journal of Physics D: Applied Physics* 2003, 36, 1609.

38. Xu, C.; Sritharan, T.; Mhaisalkar, S.; Srinivasan, M.; Zhang, S. An XPS study of Al 2 Au and AlAu 4 intermetallic oxidation. *Applied Surface Science* 2007, 253, 6217-6221.
39. Lim, D. C.; Lopez-Salido, I.; Dietsche, R.; Bubek, M.; Kim, Y. D. Size-Selectivity in the Oxidation Behaviors of Au Nanoparticles. *Angewandte Chemie International Edition* 2006, 45, 2413-2415.
40. Luo, W.; Sankar, M.; Beale, A. M.; He, Q.; Kiely, C. J.; Bruijnincx, P. C.; Weckhuysen, B. M. High performing and stable supported nano-alloys for the catalytic hydrogenation of levulinic acid to γ-valerolactone. *Nature communications* 2015, 6.
41. Mukherjee, P. Crystal structures and phase formation thermodynamics of iron-gold nanoclusters. 2013.
42. Murty, K. L.; Charit, I. *An introduction to nuclear materials: fundamentals and applications*. John Wiley & Sons: 2013.
43. McGuire, T.; Aboaf, J.; Klokholm, E. Magnetic and transport properties of Fe-Au and Co-Au films. *Journal of applied physics* 1981, 52, 2205-2207.
44. Amendola, V.; Meneghetti, M.; Bakr, O. M.; Riello, P.; Polizzi, S.; Anjum, D. H.; Fiameni, S.; Arosio, P.; Orlando, T.; de Julian Fernandez, C. Coexistence of plasmonic and magnetic properties in Au 89 Fe 11 nanoalloys. *Nanoscale* 2013, 5, 5611-5619.
45. Emmoth, B.; Braun, M. Angular Distributions of Sputtered Si and SiO2 Combined with Surface Morphology Studies. *Physica Scripta* 1981, 24, 415.
46. Niehus, H.; Heiland, W.; Taglauer, E. Low-energy ion scattering at surfaces. *Surface Science Reports* 1993, 17, 213-303.
47. Bay, H.; Bohdansky, J.; Hofer, W.; Roth, J. Angular distribution and differential sputtering yields for low-energy light-ion irradiation of polycrystalline nickel and tungsten. *Applied physics* 1980, 21, 327-333.
48. Khan, S. A.; Heinig, K.-H.; Avasthi, D. Atomistic simulations of Au-silica nanocomposite film growth. *Journal of applied physics* 2011, 109, 094312.
49. Pannu, C.; Singh, U. B.; Kumar, S.; Tripathi, A.; Kabiraj, D.; Avasthi, D. Engineering the strain in graphene layers with Au decoration. *Applied Surface Science* 2014, 308, 193-198.
50. Mahieu, S.; Leroy, W.; Van Aeken, K.; Wolter, M.; Colaux, J.; Lucas, S.; Abadias, G.; Matthys, P.; Depla, D. Sputter deposited transition metal nitrides as back electrode for CIGS solar cells. *Solar Energy* 2011, 85, 538-544.
51. Weast, R. C. Handbook of Chemistry and Physics 67th, ed. *Chemical Rubber Co., Cleveland, OH* 1987.